

A Spectral Vanishing Viscosity Method for Large-Eddy Simulations

G-S. Karamanos and G. E. Karniadakis¹

Division of Applied Mathematics, Brown University, Providence, Rhode Island 02912

E-mail: gk@cfm.brown.edu

Received October 4, 1999; revised May 30, 2000

A new simulation approach for high Reynolds number turbulent flows is developed, combining concepts of monotonicity in nonlinear conservation laws with concepts of large-eddy simulation. The spectral vanishing viscosity (SVV), first introduced by E. Tadmor [*SIAM J. Numer. Anal.* **26**, 30 (1989)], is incorporated into the Navier–Stokes equations for controlling high-wavenumber oscillations. Unlike hyperviscosity kernels, the SVV approach involves a second-order operator which can be readily implemented in standard finite element codes. In the work presented here, discretization is performed using hierarchical spectral/*hp* methods accommodating effectively an *ab initio* intrinsic scale separation. The key result is that monotonicity is enforced via SVV leading to stable discretizations without sacrificing the formal accuracy, i.e., exponential convergence, in the proposed discretization. Several examples are presented to demonstrate the effectiveness of the new approach including a comparison with eddy-viscosity spectral LES of turbulent channel flow. In its current implementation the SVV approach for controlling the small scales is decoupled from the large scales, but a procedure is proposed that will provide coupling similar to the classical LES formulation. © 2000 Academic Press

1. INTRODUCTION

Thirty years after intense research on large-eddy simulations (LES) of turbulent flows based on the eddy-viscosity subfilter models [1], there is now consensus that such an approach is subject to fundamental limitations. It has been demonstrated for a number of different flows that the shear stress and strain tensors involved in subfilter eddy-viscosity models have different topological features [2–5]. In particular, it was reported in [4] that the dynamics of the local energy flux, even in the inertial range, is poorly correlated with the locally averaged energy dissipation rate, an assumption employed in most eddy-viscosity

¹ To whom correspondence should be addressed.

models [6]. To this end, *alternative* LES formulations have been investigated based on either the filtered or the original Navier–Stokes equations.

A filtered non-eddy-viscosity approach is the scale-similarity model, first proposed by Bardina [7], and its subsequent variants (e.g., [8]). It assumes that the subfilter stress is proportional to the so-called Leonard stresses, which are expressed in terms of the filtered velocity gradients. Preliminary results with mixed models that include a dissipative component for numerical stability (e.g., see [9]) have shown significant improvement over eddy-viscosity models. However, such mixed models are typically computationally more expensive and their implementation in *complex-geometry flows* is not straightforward. Independent of this approach, there has been also an effort to abandon the classical formulation and employ instead the original (unfiltered) Navier–Stokes equations. In this case, one could use *ab initio* scale separation (see, for example, [10] and [11]) with an additional assumption for stabilization, or invoke *monotonicity* via nonlinear limiters that implicitly act as a filtering mechanism for the small scales [12–15]. Regarding the latter, the original ideas of von Neumann and Richtmyer on artificial dissipation motivated Smagorinsky in developing his model (C. Leith, private communications).

Turbulence simulations using *monotonicity-preserving* schemes have concentrated on homogeneous turbulence, employing both PPM- and FCT-type algorithms [12, 14], as well as on wall-bounded flows using FCT-based limiting [16]. Unlike other strictly monotonic discretizations of nonlinear conservation laws, which are total-variation-diminishing (TVD) and thus first-order accurate (see theorem of LeVeque and Goodman [17]), the PPM and FCT algorithms employ nonlinear limiters and guarantee monotonicity locally while preserving at least second-order accuracy in both phase and amplitude [18, 19]. These schemes honor the weaker total-variation-bounded (TVB) condition which allows for small amplitude oscillations. The intriguing feature of the monotonically integrated LES (or MILES) approach [14] is the activation of the limiter on the convective fluxes and its role in generating implicitly a tensorial form of eddy viscosity that acts to stabilize the flow and suppress oscillations. It was reported in [14] that if the resolution is fine enough to ensure that the cut-off wavenumber lies in the inertial range, then the simulation results seem to be independent of the generated viscosity.

In the aforementioned PPM and FCT algorithms for convection, use of nonlinear limiters or reconstruction procedures is in some form equivalent to adding diffusion to the hyperbolic conservation laws so that entropy dissipation is created and a unique solution is obtained (see Lax [20]). If the discretization lacks entropy dissipation, then Gibbs oscillations are produced and eventually render the solution unstable. In convection-dominated high Reynolds number flows the situation is analogous. However, this mechanism is implicit and although the induced artificial diffusion may scale with the local resolution as $\propto (\Delta x)^s$, $s > 1$, it is an uncontrollable process that may compromise the solution accuracy. This conflict between monotonicity and accuracy, first analyzed by Godunov [21], was more recently revisited by Tadmor [22], who has developed the *first theoretical result* on the convergence and stability of spectral approximations for nonlinear conservation laws [22]. Specifically, Tadmor introduced artificial dissipation via the spectral vanishing viscosity (SVV), which is sufficiently large to suppress oscillations, yet small enough not to affect the solution accuracy. In the context of spectral discretizations, for example, SVV can be viewed as a compromise between the classical TVB viscosity approximation and the exponentially accurate yet unstable spectral approximation.

The spectral vanishing viscosity approach guarantees an essentially nonoscillatory behavior although some small oscillations of *bounded amplitude* may be present in the solution. This theory is based on three key components:

1. a vanishing viscosity amplitude which decreases with the mode number;
2. a viscosity-free spectrum for the lower, most energetic modes; and
3. an appropriate viscosity kernel for the high wavenumbers.

If hierarchical discretizations are employed, the combined formulation inherits the aforementioned scale separation attempted by other authors, e.g., in the multiscale variational method of Hughes [11] or in the nonlinear Galerkin method of Temam [10]. On the other hand, monotonicity of the TVB kind is preserved, but the high-frequency regularization employed is controlled by parameters whose range is given directly by the theory. This theory has been extended to spectral collocation discretizations in [23] and to superviscosity formulations, first by Tadmor [24] and more recently by Ma [25, 26], in order to extend the range of the *viscosity-free* spectrum.

All applications of the SVV method so far deal with one-dimensional conservation laws apart from the work of Andreassen *et al.* [27], who have used SVV for two-dimensional simulations of waves in a stratified atmosphere; see also [28] for two-dimensional examples for the Euler equations. Standard Fourier or Legendre discretizations were employed by Tadmor and his colleagues while Chebyshev discretization was employed by Andreassen *et al.* In the current work, the SVV concept is used in the context of simulating incompressible turbulent flows using multidomain spectral methods, based on the spectral/*hp* Galerkin approach (see Appendix I and [29]). The equations used are the unfiltered Navier–Stokes equations which are enhanced on the right-hand side with a spectral vanishing viscous operator. For underresolved or marginally resolved simulations, rapid-solution variations appear as discontinuity as sketched in Fig. 1 and this can be described locally by an inviscid Burgers-type equation. For standard Fourier methods and simulations of homogeneous turbulence, SVV can be thought of as using hyperviscous dissipation that will affect only the high Fourier modes. This approach has been used successfully, for example, by Borue and Orszag [4] in achieving high Reynolds number simulations. The proposed method extends such capability to complex-geometry discretizations using a standard finite element framework. To this end, superviscous operators are not used, as they cannot be handled in the standard Galerkin framework that requires C^0 continuity for the trial basis. We note, however, that discontinuous Galerkin methods can handle high-order SVV operators, but at higher computational complexity.

It is worth pointing out an important distinction between the classical LES formulation and the currently proposed SVV formulation. In particular, unlike standard large-eddy formulations where the small-scale dynamics is coupled to the dynamics of the large scales with explicit contributions from the subgrid scales, in the current implementation the SVV approach ignores this coupling. This rather strong assumption is also typical of other monotonicity-based LES approaches; however, in the SVV approach a coupling similar to eddy viscosity subgrid models can be implemented, and it will be discussed in Section 6.

In the current paper, the SVV method is first extended to spectral discretizations using general Jacobi polynomials, in single and multiple domains, with solutions of the Burgers equations compared to previously published results; the emphasis is on the performance of SVV using multidomains. An SVV-based formulation is then developed for the two-dimensional Navier–Stokes equation concentrating on preserving spectral accuracy. The

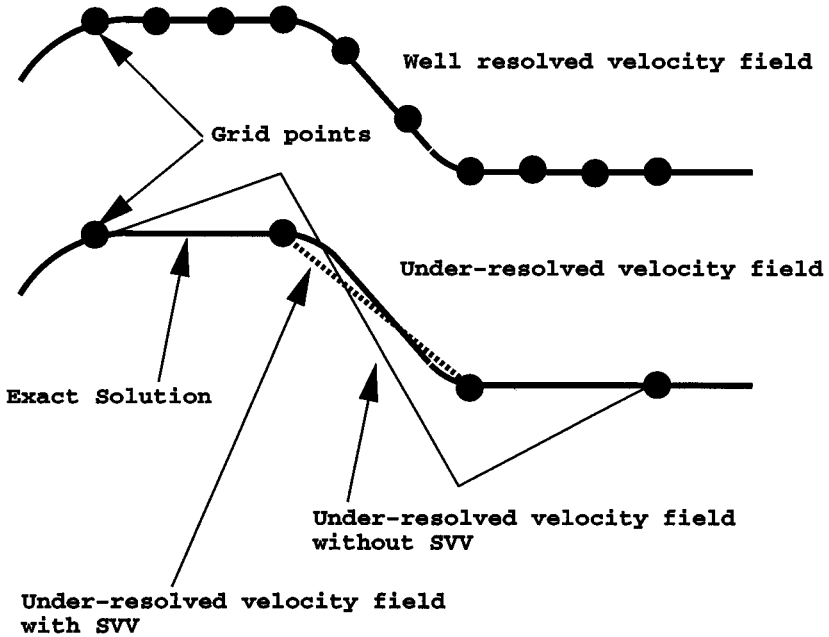


FIG. 1. Although a well-resolved velocity field may be smooth, when it is underresolved, the discretization may interpret a variation as a discontinuity. In these cases, SVV may be introduced in order to damp the oscillations and reproduce a smooth velocity field.

Kovasznay flow [29] is simulated to investigate the effect of the SVV method on the solution accuracy. Finally, the new method is applied to simulations of the standard three-dimensional turbulent channel flows at Reynolds numbers 180 and 395 (based on wall shear velocity). We conclude with a brief discussion on possible extensions of the proposed methodology, including a strategy for coupling the SVV approach to the dynamics of large scales.

2. THE SPECTRAL VANISHING VISCOSITY METHOD

Tadmor [22] first introduced the concept of SVV using the inviscid Burgers equation

$$\frac{\partial}{\partial t} u(x, t) + \frac{\partial}{\partial x} \left(\frac{u^2(x, t)}{2} \right) = 0, \quad (1)$$

subject to given initial and boundary conditions. The distinct feature of solutions to this problem is that spontaneous jump discontinuities (shock waves) may be developed, and hence a class of weak solutions can be admitted. Within this class, there are many possible solutions, and in order to single out the physically relevant one an additional entropy condition is applied, of the form

$$\frac{\partial}{\partial t} \left(\frac{u^2(x, t)}{2} \right) + \frac{\partial}{\partial x} \left(\frac{u^3(x, t)}{3} \right) \leq 0. \quad (2)$$

In practical applications, spectral methods are often augmented with smoothing procedures in order to reduce the Gibbs oscillations [30] associated with discontinuities arising at the domain boundaries or due to underresolution. However, with nonlinear problems,

convergence of the Fourier method, for example, may fail despite additional smoothing of the solution. Tadmor [22] introduced the SVV method, which adds a small amount of controlled dissipation that satisfies the entropy condition, yet retains spectral accuracy. It is based on viscosity solutions of nonlinear Hamilton–Jacobi equations, which have been studied systematically in [31]. Specifically, the viscosity solution for the Burgers equation has the form

$$\frac{\partial}{\partial t} u(x, t) + \frac{\partial}{\partial x} \left(\frac{u^2(x, t)}{2} \right) = \epsilon \frac{\partial}{\partial x} \left[Q_\epsilon \frac{\partial u}{\partial x} \right], \quad (3)$$

where $\epsilon (\rightarrow 0)$ is a viscosity amplitude and Q_ϵ is a viscosity kernel, which may be nonlinear and, in general, a function of x . Convergence may then be established by compactness estimates combined with entropy dissipation arguments [22]. To respect spectral accuracy, the SVV method makes use of viscous regularization and Eq. (3) may be rewritten in discrete form (retaining N modes) as

$$\frac{\partial}{\partial t} u_N(x, t) + \frac{\partial}{\partial x} \left[\mathcal{P}_N \left(\frac{u^2(x, t)}{2} \right) \right] = \epsilon \frac{\partial}{\partial x} \left[Q_N * \frac{\partial u_N}{\partial x} \right], \quad (4)$$

where the star (*) denotes convolution and \mathcal{P}_N is a projection operator. Q_N is a (possibly nonlinear) viscosity kernel, which is only activated for high wave numbers. In Fourier space, this kind of spectral viscosity can be efficiently implemented as multiplication of the Fourier coefficients of u_N with the Fourier coefficients of the kernel Q_N , i.e.,

$$\epsilon \frac{\partial}{\partial x} \left[Q_N * \frac{\partial u_N}{\partial x} \right] = -\epsilon \sum_{M \leq |k| \leq N} k^2 \hat{Q}_k(t) \hat{u}_k(t) e^{ikx},$$

where k is the wavenumber, N the number of Fourier modes, and M the wavenumber above which the SVV is activated.

Originally, Tadmor [22] used

$$\hat{Q}_k = \begin{cases} 0, & |k| \leq M \\ 1, & |k| > M, \end{cases} \quad (5)$$

with $\epsilon M \sim 0.25$ based on the consideration of minimizing the total variation of the numerical solution. In subsequent work, however, a smooth kernel was used, since it was found that the C^∞ smoothness of \hat{Q}_k improves the resolution of the SVV method. For Legendre pseudo-spectral methods, Maday *et al.* [32] used $\epsilon \approx N^{-1}$, activated for modes $k > M \approx 5\sqrt{N}$, with

$$\hat{Q}_k = e^{-\frac{(k-N)^2}{(k-M)^2}}, \quad k > M. \quad (6)$$

In order to see the difference between the convolution operator on the right-hand side in Eq. (4) and the usual viscosity regularization, following Tadmor [33], we expand as

$$\epsilon \frac{\partial}{\partial x} \left[Q_N * \frac{\partial u_N}{\partial x} \right] = \epsilon \frac{\partial^2 u_N}{\partial x^2} - \epsilon \frac{\partial}{\partial x} \left[R_N(x, t) * \frac{\partial u_N}{\partial x} \right], \quad (7)$$

where

$$R_N(x, t) \equiv \sum_{k=-N}^N \hat{R}_k(t) e^{ikx}; \quad \hat{R}_k(t) \equiv \begin{cases} 1 - \hat{Q}_k(t) & |k| \geq M \\ 1 & |k| < M. \end{cases} \quad (8)$$

The extra term appearing in addition to the first standard viscosity term makes this method different. It measures the distance between the spectral (vanishing) viscosity and the standard viscosity. This term is bounded in the L_2 norm similarly to the spectral projection error. In this paper we refer to the viscosity as vanishing, as the theory requires that

$$\epsilon \approx \frac{1}{N^\theta \log N}, \quad \theta \leq 1$$

and thus $\epsilon \rightarrow 0$ for high wavenumbers. In more recent work, Tadmor and his collaborators [23] refer to it as simply *spectral viscosity*, but this terminology may be confused with the one used by Lesieur and his group [34].

At this point it is also instructive to compare the spectral vanishing viscosity to the aforementioned spectral eddy viscosity introduced by Kraichnan [35] and Chollet–Lesieur [34, 36]. The latter has the nondimensional form [36]

$$\nu(k/N) = K_0^{-3/2} [0.441 + 15.2 \exp(-3.03N/k)], \quad K_0 = 2.1. \quad (9)$$

Comparing the Fourier analog of this eddy viscosity employed in LES [34] to the viscosity kernel $Q_k(k, M, N)$ introduced in the SVV method, Fig. 2 shows both viscosity kernels normalized by their maximum value at $k = N$. For SVV, two different values of the cut-off wavenumber are considered,

$$M = C\sqrt{N} \quad \text{for } C = 0 \text{ and } C = 5. \quad (10)$$

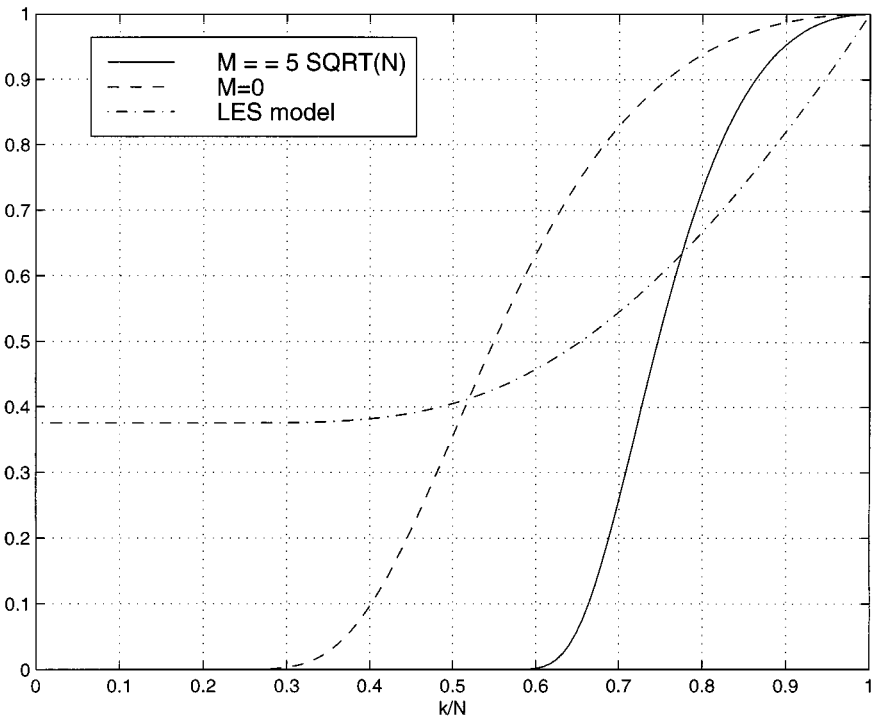


FIG. 2. Normalized viscosity kernels for the spectral vanishing viscosity (dashed line $C = 0$ and solid line $C = 5$) and the Kraichnan/Chollet–Lesieur viscosity (dash-dot line).

This range has been used in most of the numerical experiments so far (see, for example, [27, 32]) and is consistent with the theoretical results [22]. In the plot it is shown that, in general, the two forms of viscosity have similar distributions, but the SVV form does not affect the first one-third or one-half of the spectrum (viscosity-free portion) and it increases faster than the Kraichnan/Chollet–Lesieur eddy viscosity in the higher wavenumber range, e.g., in the second-half of the spectrum.

3. EXPERIMENTS WITH 1-D BURGERS' EQUATION

One-dimensional results are first presented, applying the SVV method to inviscid Burgers' equation in order to assess the range of the parameters involved in the viscosity kernel. The more general multidomain discretization is reviewed in Appendix I, i.e., the spectral/ hp element method. A multidomain implementation for nonlinear hyperbolic problems has also been reported in [37].²

The Fourier method as well as the spectral/ hp element method with SVV is applied to the periodic inviscid Burgers equation, using

$$u(x, t = 0) = \sin(\pi x)$$

as initial conditions. The domain considered extends from $-1 \leq x \leq 1$, and a smooth kernel Q_N is used.

3.1. SVV–Fourier Spectral Method: Results

The SVV method is first briefly presented with the Fourier method, as proposed by Chen *et al.* [24a]. Here $\epsilon \approx N^{-1}$ and $M \approx 2N^{1/2}$ are used, with the Burgers equation integrated up to time $t = 1.0$. Figure 3 shows the effect of the SVV method on the 1-D Burgers solution, for different values of ϵ , with a C^∞ kernel Q_k . It is clear that with the introduction of SVV, the solution converges strongly in L^p for $p < \infty$ (but not uniformly) to the exact entropy solution, in sharp contrast to the oscillatory behavior of the viscosity-free Fourier method. A third-order Adams–Bashforth time-stepping scheme is used, with a time step $\Delta t = 0.001$. It should be noted that with $\epsilon = 0$ the solution diverges. This is somewhat obvious from the plot, which shows that as the viscosity amplitude decreases *below the theoretical limit*, the amplitude of the oscillations increases significantly. It is also noted that the aforementioned *spectral convergence* is not obvious in this stable, but still wiggly solution. To recover spectral convergence, further postprocessing is required to eliminate the still visible Gibbs phenomenon. This, for example, can be obtained by reconstruction as documented in [38], in conjunction with an edge detection technique; this has been successfully demonstrated by Gelb and Tadmor [39]. No postprocessing or other type of reconstruction is necessary at each time step, but only at the final time step, allowing this method to be particularly efficient.

3.2. SVV–Jacobi Spectral Method: Results

Next, the global spectral method (single domain) is employed using $P = 64$ hierarchical Jacobi modes as the basis (see Appendix I), and repeat the previous experiment. In Fig. 4

² We thank the anonymous referee for suggesting this unpublished work.

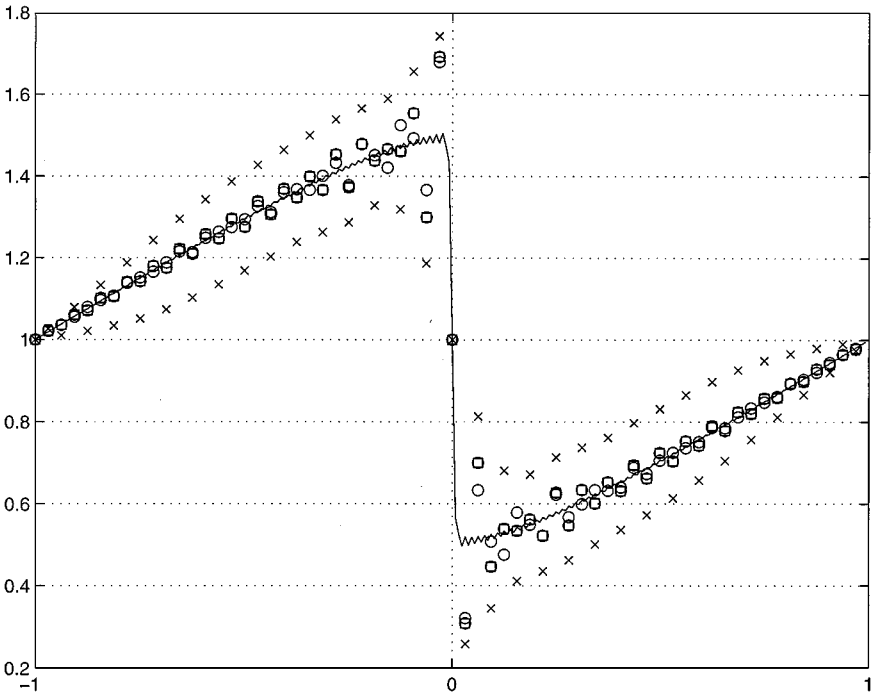


FIG. 3. Solution of 1-D Burgers' equation with $N = 64$ Fourier modes and $M = 16 = 2\sqrt{N}$: solid line—very high resolution (512 modes); circles— $\epsilon = 1/N$; squares— $\epsilon = 1/2N$; crosses— $\epsilon = 1/5N$.

results from these simulations are shown with different values of ϵ and M used; the Fourier method for $N = 64$ is also included for reference. It is clear that as ϵ increases, the amplitude of oscillations decreases. By increasing the cut-off wavenumber M the amplitude increases, although the amplitude is more sensitive to changes in ϵ rather than M .

3.3. SVV-Jacobi Spectral/hp Element Method: Results

Multidomain discretization (see Appendix I) is next investigated with the same test case performed with $K = 2$ and $K = 3$ elements (Fig. 5). For the 2-element case $P = 32$ is used, while the 3-element case uses $P = 21$. Overall, similar behavior to that with the 1-element case is noted. For 3 elements (Fig. 5, right), there is improvement similar to that with the use of the SVV method. Comparing the results of Figs. 4 and 5 reveals that as the number of elements increases the discretization is more stable even without the incorporation of SVV.

3.4. Conclusion

The numerical experiments with the 1-D Burgers equation indicate stability consistent with the theory and the suggested range of parameters. The scaling with respect to ϵ and M is consistent with the theoretical prediction. In the multidomain discretization many more experiments are required to rigorously define trends that cannot be predicted by the theory. However, it is evident from these experiments that comparable accuracy may be obtained using parameterizations similar to those used for the Fourier method.

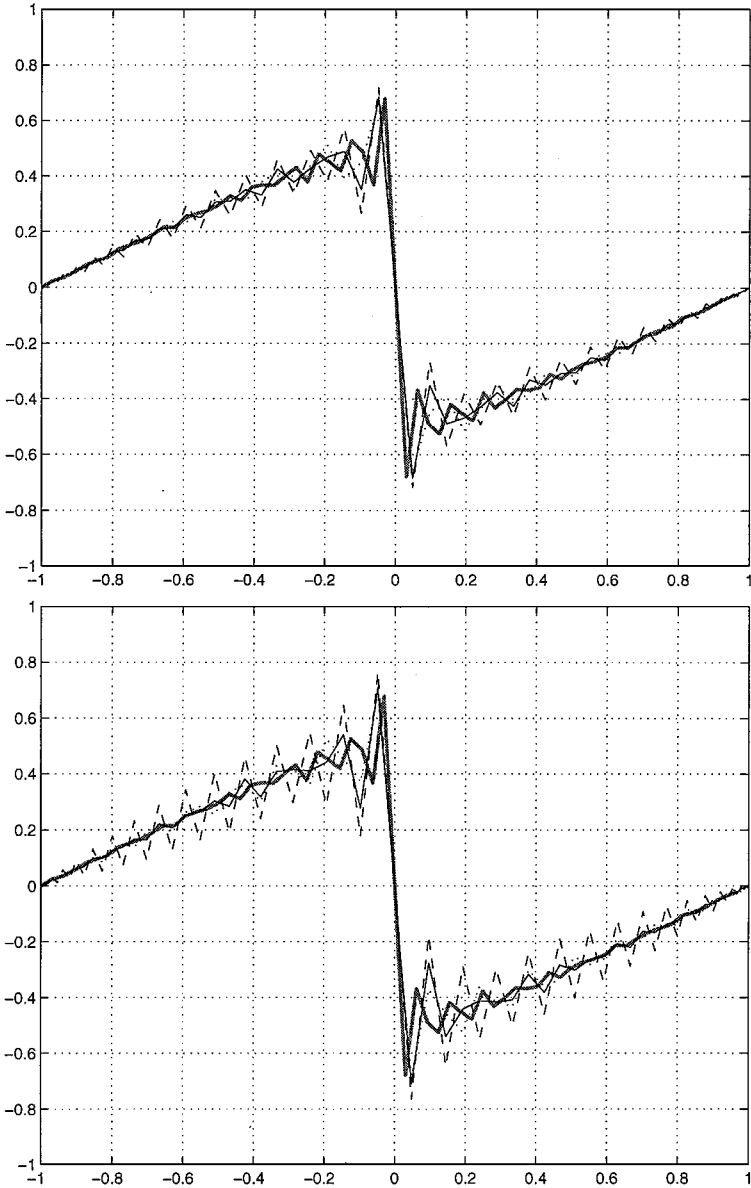


FIG. 4. One-element discretization. Top: $P = 64$; $M = 16 = 2\sqrt{P}$. Solid thick line: Fourier discretization— $\epsilon = 1/P$; solid thin line: Jacobi discretization— $\epsilon = 1/P$; dashed line: Jacobi discretization— $\epsilon = 1/2P$; dotted line: Jacobi discretization— $\epsilon = 2/P$. Bottom: $P = 64$; $M = 26$. Same legend as the plot on the top. (P is the number of Jacobi modes.)

4. CONVERGENCE FOR 2-D NAVIER-STOKES EQUATIONS

The main discretization steps of the incompressible Navier–Stokes equations are summarized in Appendix II. The main point is that the SVV operator can be treated similarly to the variable viscosity operator in traditional LES [40]. It is noted that the resolution per element (spectral order P) may vary and so do the SVV parameters. The 2-D spatial discretization is similar to the 1-D case (see Appendix I) since a tensor product

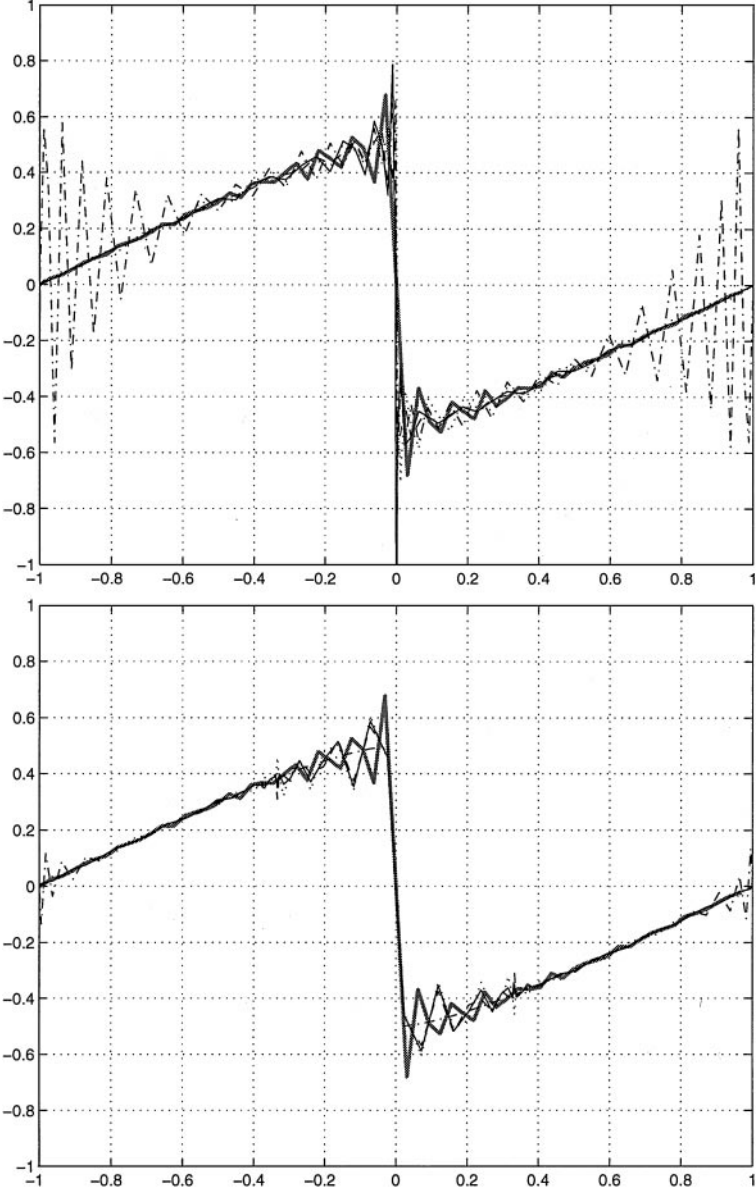


FIG. 5. Top: Two-element discretization $P = 32$; $M = 11 = 2\sqrt{P}$. Solid thick line: Fourier discretization— $\epsilon = 1/P$; solid thin line: Jacobi discretization— $\epsilon = 1/P$; dashed line: Jacobi discretization— $\epsilon = 1/2P$; dotted line: Jacobi discretization— $\epsilon = 2/P$. Dash-Dot line: Jacobi discretization— $\epsilon = 0$. Bottom: Three-element discretization $P = 21$; $M = 9 = 2\sqrt{P}$. Same legend as the plot on the top. (P is the number of Jacobi modes per element.)

rule is employed to obtain the 2-D trial basis including triangular domains (see [29] for details). Similarly, the one-dimensional formulation of the SVV method may be extended to two dimensions for quadrilateral and triangular elements by redefining the kernel Q_p as

$$Q_p = e^{-\left(\frac{(p_x - P_x)(p_x - P_x)}{(p_x - M_x)(p_x - M_x)} + \frac{(p_y - P_y)(p_y - P_y)}{(p_y - M_y)(p_y - M_y)}\right)}, \quad M_x < p_x \leq P_x, \quad M_y < p_y \leq P_y. \quad (11)$$

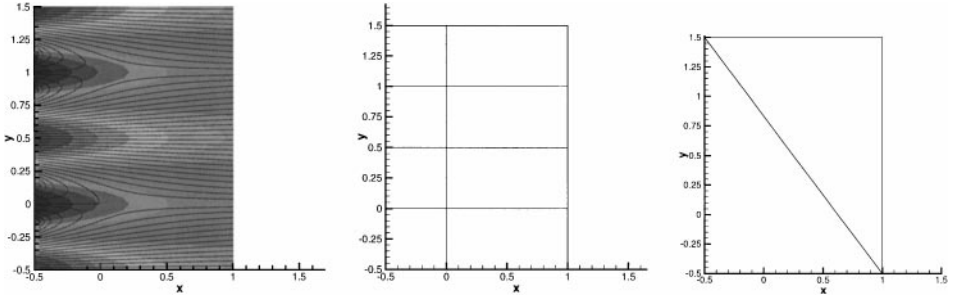


FIG. 6. Streamline pattern (left) and quadrilateral and triangular mesh (center and right, respectively) for the Kovaszny flow. Streamwise velocity contours are superimposed on the streamlines pattern.

In order to numerically validate the 2-D methodology, the 1-D Burgers equation was applied to a 2-D domain, with an initial condition $u(x, y, t = 0) = \sin(\pi x) + \sin(\pi y)$, in a $-1 \leq x \leq 1$, $-1 \leq y \leq 1$ domain. For an isotropic mesh, the two directions are identical, and results identical to the 1-D results were obtained.

In order to evaluate the effect of SVV on the quality of Navier–Stokes solutions, the exact Kovaszny solution is employed for laminar flow behind a two-dimensional grid (see [29, Chap. 9]). The solution is a function of the Reynolds number, Re , and is of the form

$$u = 1 - e^{\lambda x} \cos(2\pi y), \quad v = \frac{1}{2\pi} e^{\lambda x} \sin(2\pi y),$$

where $\lambda = Re^2/2 - (Re^2/4 + 4\pi^2)^{0.5}$. All boundary conditions are Dirichlet conditions, defined by the above exact solution.

Two domains are employed, one consisting of 8 quadrilateral elements and one consisting of 2 triangular elements shown in Fig. 6. The computed steady-state streamline pattern is plotted in Fig. 6 (left) at $Re = 40$. A parametric study on ϵ and M is conducted, with emphasis placed on the effect of the SVV method on the accuracy. The results are summarized in Table I. Using $K = 1, 4$ and $K = 8$ elements, it is clear that the SVV method either improves or retains the accuracy of the solution. It is important to note that the addition of SVV to the Navier–Stokes equations does not affect adversely the convergence rate. Due to the smooth character of the Kovaszny flow, spectral accuracy may be achieved very quickly. This is documented in the convergence plot shown in Fig. 7. In order to contrast the results with the traditional artificial dissipation method, the solution is also computed by keeping only the first term in Eq. (7). We see that the error decays extremely slowly in this case. Therefore, *the remaining term in the convolution in Eq. (7) is important in guaranteeing spectral convergence as argued by the theory* [22].

This test case is important, as it indicates the minimal effect of the SVV method in smooth well-resolved regions if the theoretically predicted parameters are used. Furthermore, at low resolutions, enhanced accuracy is achieved.

5. SVV SIMULATIONS OF TURBULENT CHANNEL FLOWS

The extension of the SVV method to three dimensions is straightforward using tensor products. The effectiveness of the SVV spectral method is evaluated in the context of turbulent channel flow. To this end, a Fourier discretization is used along the flow direction and spectral/ hp quadrilateral elements in the cross-flow and wall-normal directions.

TABLE I
Kovaszny Flow

P	Elements	ϵ	M	L_∞ error	L_2 error	H_1 error
10	1 (Quads)	0.0	0	0.2182	0.089	0.855
10	1 (Quads)	1/P	5	0.217	0.088	0.85
16	1 (Quads)	0.0	0	0.001164	0.00039	0.0069
16	1 (Quads)	1/P	8	0.00113	0.00038	0.0068
18	1 (Quads)	0.0	0	0.00018	4.99E-5	0.000967
18	1 (Quads)	1/P	9	0.000176	4.98E-5	0.000946
7	4 (Quads)	0.0	0	0.00319	0.014	0.0179
7	4 (Quads)	1/P	4	0.00319	0.014	0.0179
11	4 (Quads)	0.0	0	5.1172E-5	1.93E-5	0.00018
11	4 (Quads)	1/P	7	5.1172E-5	1.93E-5	0.00018
7	8 (Quads)	0.0	0	0.000245	8.57E-5	0.00226
7	8 (Quads)	1/P	3	0.000245	8.57E-5	0.00226
10	1 (Triangles)	0.0	0	0.2062	0.0906	0.817
10	1 (Triangles)	1/P	5	0.2058	0.0904	0.8149
16	1 (Triangles)	0.0	0	0.008	0.00105	0.0224
16	1 (Triangles)	1/P	8	0.0079	0.00105	0.0223
18	1 (Triangles)	0.0	0	0.001749	0.000179	0.0045
18	1 (Triangles)	1/P	9	0.001746	0.000179	0.0045

Note. This smooth solution demonstrates that the addition of spectral vanishing viscosity does not affect adversely the exponential convergence of the spectral element/ hp discretization.

5.1. Results at $Re_\tau = 180$

Channel flow at $Re_\tau = 180$ is simulated, with periodic boundary conditions in the stream-wise and spanwise directions following the benchmark solutions of Kim *et al.* [41]. Figure 8 shows the computational domain used, with $L_x = 5$, $L_y = 2$, and $L_z = 2$. Two different meshes are used; the first one (Table II) has $K = 4$ elements in the cross-flow plane, with uniform $P = 21$ in all elements. In the streamwise direction 16 Fourier modes are employed. This translates to *average* resolution of $\Delta x^+ = 56$, $\Delta z^+ = 26$, $\Delta y^+ = 26$. The second mesh (Table II) has $K = 25$ elements in the cross-flow plane, with polynomial

TABLE II
Test Cases for Channel Flow at $Re_\tau = 180$

Case	Elements	ϵ	M	P
1	4	0.0	0	21
2	4	1/21	15	21
3	25	0.0	0	21
4	25	1/21	15	21
5	4	1/21	10	21
6	4	1/21	18	21
7	4	1/42	15	21
8	4	2/21	15	21

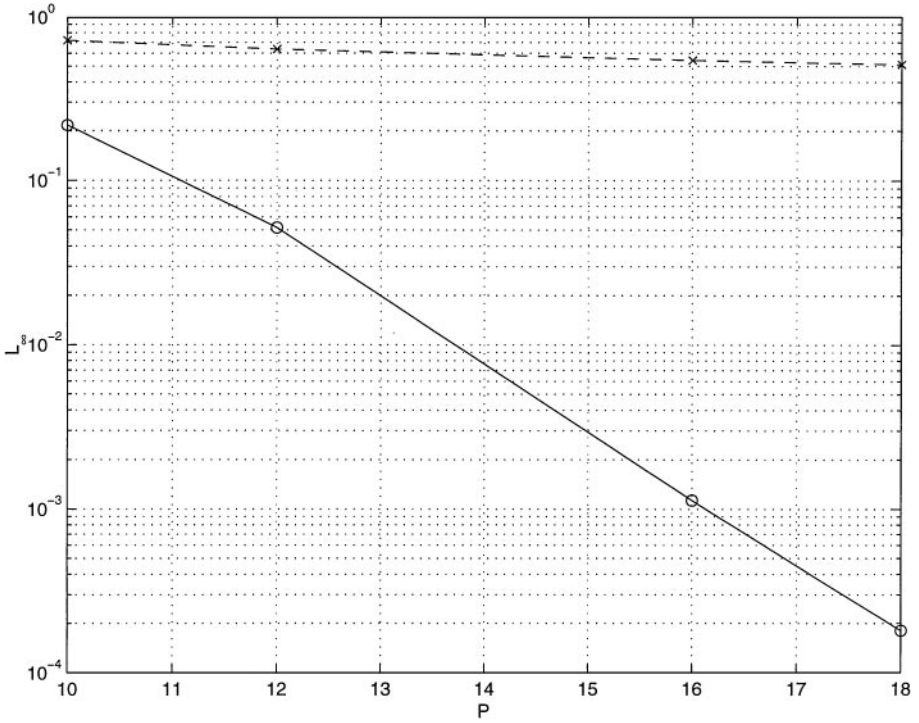


FIG. 7. Spectral (exponential) convergence is demonstrated for the exact Kovasznay Navier–Stokes solution using the SVV method. Plotted with solid line is the maximum pointwise error versus the spectral order (Jacobi polynomial degree). The dashed line shows the error if the standard artificial dissipation method is followed corresponding to the first term of the right-hand side in Eq. (7).

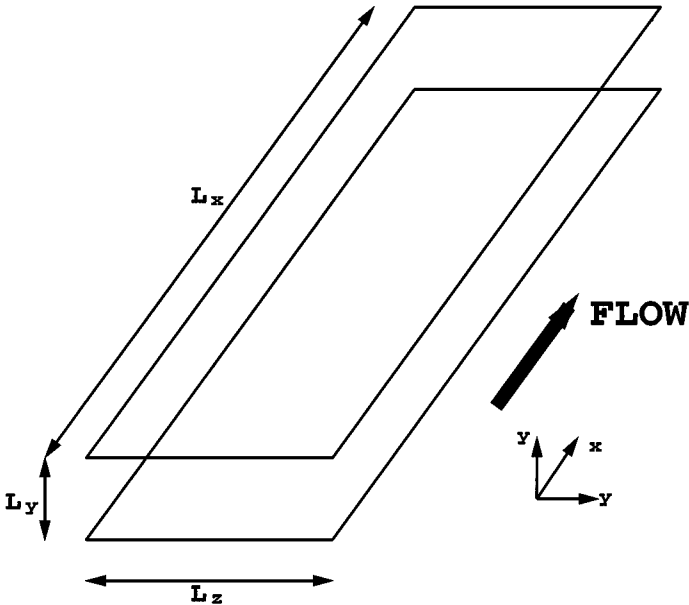


FIG. 8. Computational domain for channel flow at $Re_\tau = 180$.

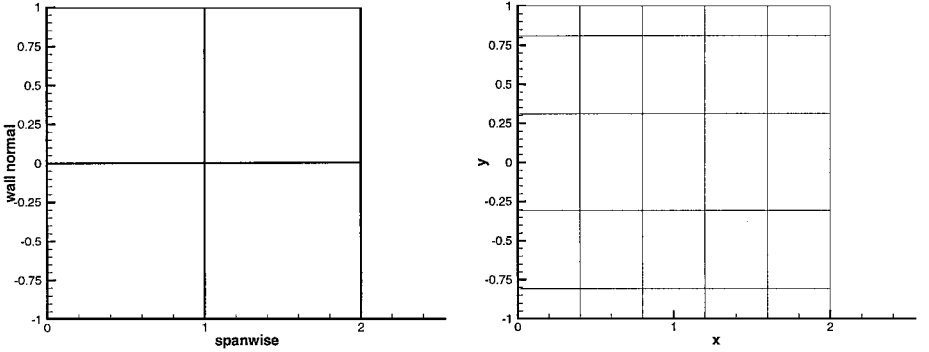


FIG. 9. Cross-flow plane for channel flow at $Re_\tau = 180$: Left, mesh 1; right, mesh 2.

order $P = 21$. This translates to *average* resolution of $\Delta z^+ = 11$, $\Delta y^+ = 11$. The same resolution is used in the streamwise direction as for mesh 1 (Fig. 9).

In the benchmark DNS of Kim *et al.* [41], the grid resolution was very fine, with a $192 \times 129 \times 160$ grid on a domain of $4\pi \times 2 \times 2\pi$, resulting in $\Delta x^+ = 12$, $\Delta z^+ = 7$ and a maximum wall-normal spacing of $\Delta y_{max}^+ = 4.4$. It was shown that most of the energetic scales were resolved even though the resolved scales were larger than the Kolmogorov scale of 2 wall units. As far as other work is concerned, the finest mesh used in [42] was $\Delta x^+ = 35$, $\Delta z^+ = 18$, $\Delta y^+ > 0.5$, while in [43] it was $\Delta x^+ = 17$, $\Delta z^+ = 5.8$, $2.1 < \Delta y^+ < 10.8$. Both simulations were using eddy-viscosity models, and the results were close to those of the available DNS.

The initial field used in the current work has been interpolated from simulations of earlier eddy-viscosity spectral LES [40]. A three-dimensional mesh (see Fig. 10) was used consisting of $K = 200$ prismatic elements with triangular base in the cross-flow plane, at spectral order $P = 5$, for a computational domain of $L_x = 13$, $L_y = 2$, $L_z = 6$. The resulting *average* resolution is $\Delta x^+ = 108$, $\Delta z^+ = 45$ and $2.83 < \Delta y^+ < 25$. A Smagorinsky constant of $c_s = 0.032$, with a Panton wall damping function [44], was applied. Some details of this LES approach with a modified subfilter model to account for the *subcell* resolution discretization (in each element) are presented in Appendix III. In the spectral element/*hp* LES subcell resolution is possible by increasing the polynomial order, and thus an appropriate equivalent length scale needs to be defined as shown in Appendix III.

5.1.1. Baseline simulations. First, two simulations are performed for each mesh, one without SVV, and one with $\epsilon = 1/P$ and $M = 15$; i.e., $M \approx 3\sqrt{P}$. The interpolated fields were integrated in time for 50 convective time units. Statistics were gathered for the last convective 20 time units. With regard to the mean streamwise velocity profiles, the differences are rather small and agree with the results of [41]. Here a comparison of turbulence intensities is presented. In Figs. 11 and 12 all components of turbulence intensities are

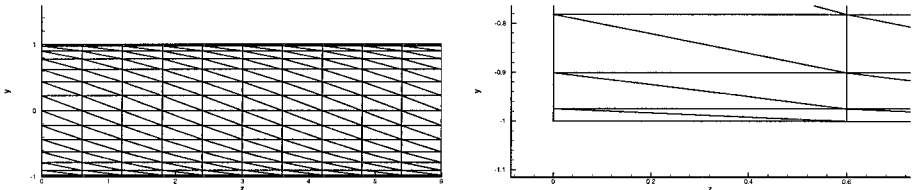


FIG. 10. Left: Mesh for Smagorinsky spectral LES. Right: Detail of near-wall mesh.

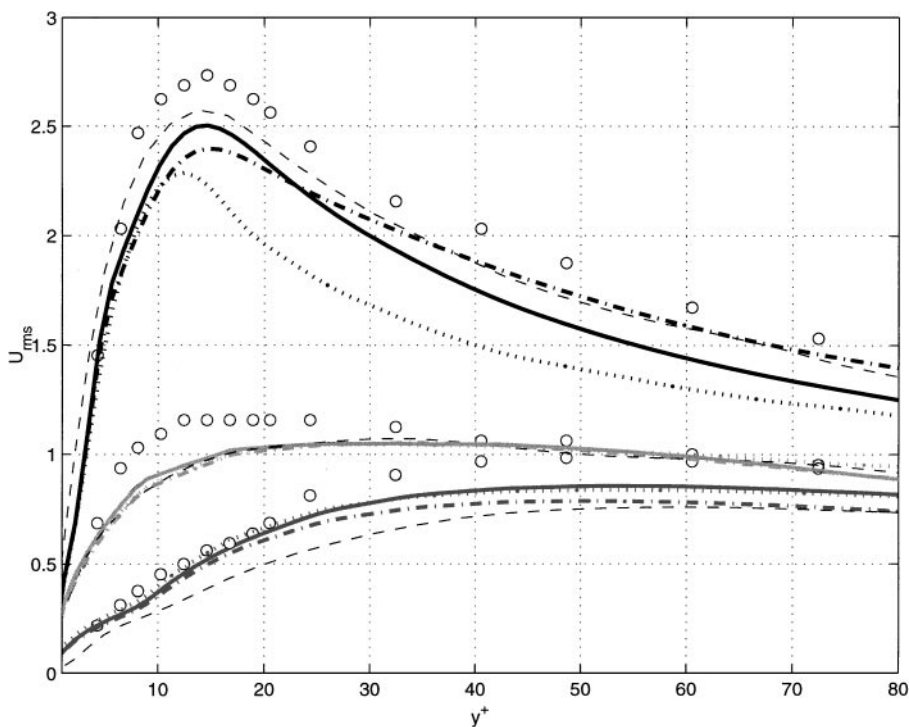


FIG. 11. Low-resolution, mesh 1: Turbulence intensities. Dotted line—no SVV; solid line—SVV/Filter; dash-dot—SVV; dashed line—spectral LES; circles—Kreplin and Eckelmann [45] at $Re_\tau = 194$.

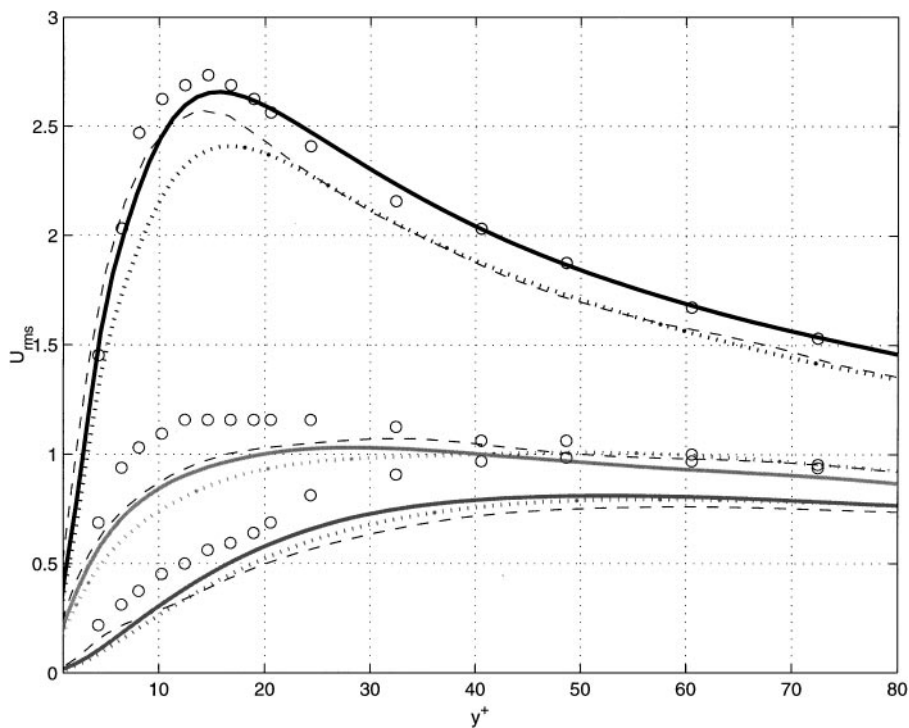


FIG. 12. High-resolution, mesh 2: Turbulence intensities. Dotted line—no SVV; solid line—SVV/filter; dashed line—spectral LES; circles—Kreplin and Eckelmann [45] at $Re_\tau = 194$.

compared against the experimental results of Kreplin and Eckelmann [45] and against the spectral LES of [40]. For cases 1 and 2 of Table II (Fig. 11), the turbulence intensities increase substantially in the streamwise and spanwise directions by introducing SVV, while in the wall-normal direction the effect is less. The general trend noted is an increase of the turbulence intensities toward the experimental data of Kreplin and Eckelmann [45], which were obtained at $Re_\tau = 194$. A similar trend is also noted for mesh 2 (Fig. 12), where in this case the SVV simulation results better match the experimental data.

Also in Fig. 11 simulation results with the SVV approach implemented in all three directions are compared against the case where the SVV approach is used in the spectral element planes (cross-flow only) with slight Gaussian filtering applied to the upper one-third of the Fourier modes in the streamwise direction. This is indicated with the dash-dot versus the solid line in the plot, respectively. We see that there are some differences, but the differences with the simulations without the SVV (dot line) are much greater. For the finer resolution case (Fig. 12) the spectral element planes and there is slight filtering in the streamwise direction. In this latter case the SVV results are clearly superior to the spectral LES results of [40].

In Fig. 13, the SVV results for meshes 1 and 2 are plotted against the benchmark DNS results of Kim *et al.* [41]. The experimental data and the spectral LES results of [40] are also included, with the high-resolution SVV simulation being in good agreement with the DNS.

5.1.2. Effects of SVV parameters. Four additional simulations for the low-resolution (i.e., 4 elements; see cases 5–8 in Table II), were also performed corresponding to variations

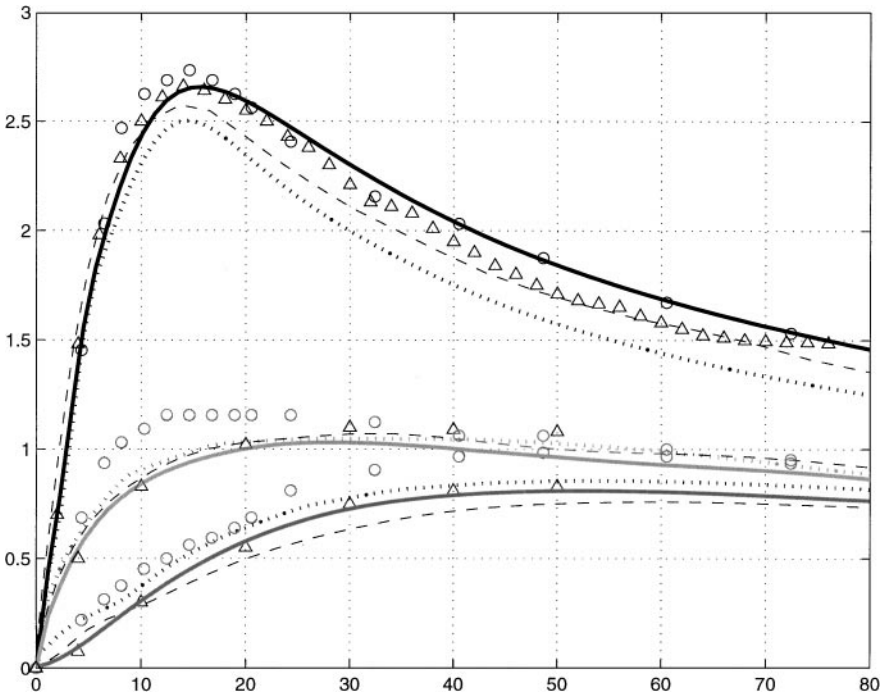


FIG. 13. Comparisons with DNS and experiments: Turbulence intensities. Dotted line—low-resolution (mesh 1) SVV; solid line—high-resolution (mesh 2) SVV; dashed line—spectral LES; circles—Kreplin and Eckelmann [45] at $Re_\tau = 194$; Triangles—Kim *et al.* [41].

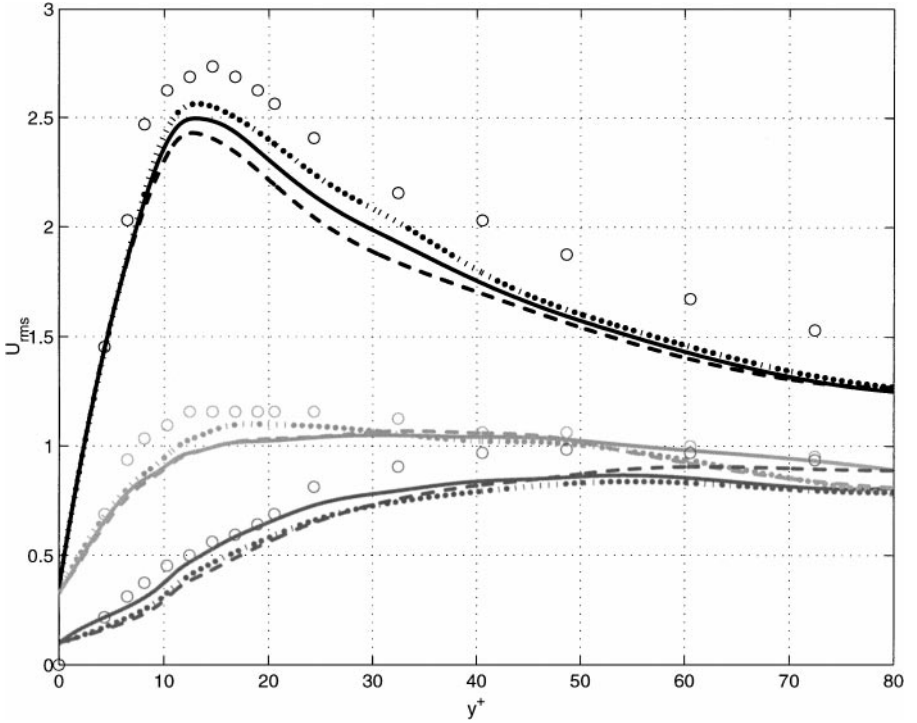


FIG. 14. Effect of wavenumber cut-off (low resolution): Turbulence intensities. Solid line— $M = 15$; dashed line— $M = 18$; dotted line— $M = 10$; circles—Kreplin and Eckelmann [45] at $Re_\tau = 194$.

of the wavenumber cut-off M and the amplitude of the SVV viscosity ϵ . In Fig. 14 we plot the results for cases 5 and 6 in Table II corresponding to $M = 10$ (dot line) and $M = 18$ (dash line) and compare against the standard case 2 (solid line). The trends with respect to this parameter are mixed: The streamwise turbulence fluctuations increase with lowering cut-off and decrease for higher cut-off values and so do the spanwise turbulence fluctuations. However, this monotonic trend does not hold for the wall-normal turbulence fluctuations. In Fig. 15 we plot cases 7 and 8 of Table II corresponding to $\epsilon = 1/42$ (dot line) and $\epsilon = 2/21$ (dash line), respectively. Again the trends are mixed for the three different components, but at least for the streamwise turbulence fluctuations the trends are consistent with the variation of the wavenumber cut-off. In particular, as the effect of SVV is enhanced, the streamwise turbulence intensity is closer to the experimental results. Clearly, we cannot draw general conclusions from these low-resolution simulations and more extensive studies concentrating on the effects of SVV parameters would provide empirical rules for the selection of optimum values of M and ϵ .

5.1.3. Computational cost. With regard to computational complexity and associated cost, the SVV simulations involve an extra matrix-vector multiply which corresponds to an overhead of about 1% compared to the cost of simulations without SVV. In contrast, in spectral eddy-viscosity LES the overhead cost is approximately 25% [40].

5.2. Results at $Re_\tau = 395$

A simulation at higher $Re_\tau = 395$ is also performed and compared to DNS of Moser *et al.* [2] at the same Reynolds numbers. A computational domain of $2\pi\delta \times 3 \times 2$ is used in

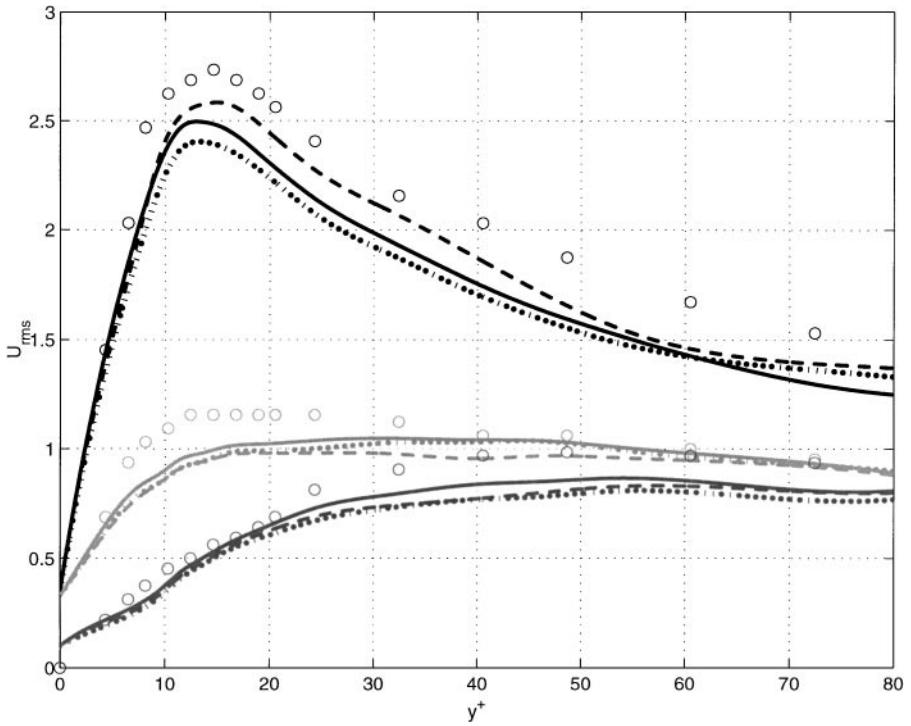


FIG. 15. Effect of SVV amplitude (low-resolution): Turbulence intensities. Solid line— $\epsilon = 1/21$; dashed line— $\epsilon = 2/21$; dotted line— $\epsilon = 1/42$; circles—Kreplin and Eckelmann [45] at $\text{Re}_\tau = 194$.

the streamwise, spanwise, and wall-normal directions, respectively, using the mesh shown in Fig. 16. A polynomial order of $P = 21$ is used, with 64 Fourier modes in the streamwise direction. The resulting *average* resolution is $\Delta x^+ = 10$, $\Delta z^+ = 6.5$, and $\Delta y^+ = 11.6$ at the centerline.

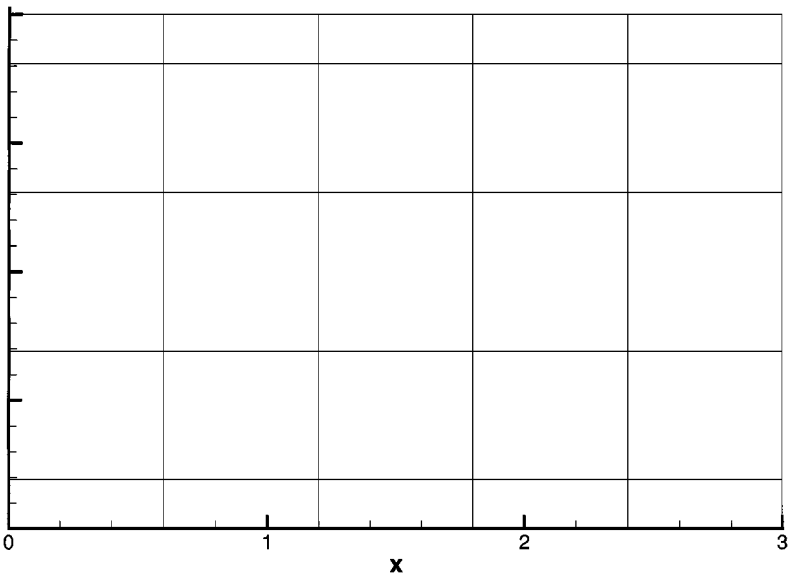


FIG. 16. Cross-flow plane for channel flow at $\text{Re}_\tau = 395$. The spectral order is $P = 21$.

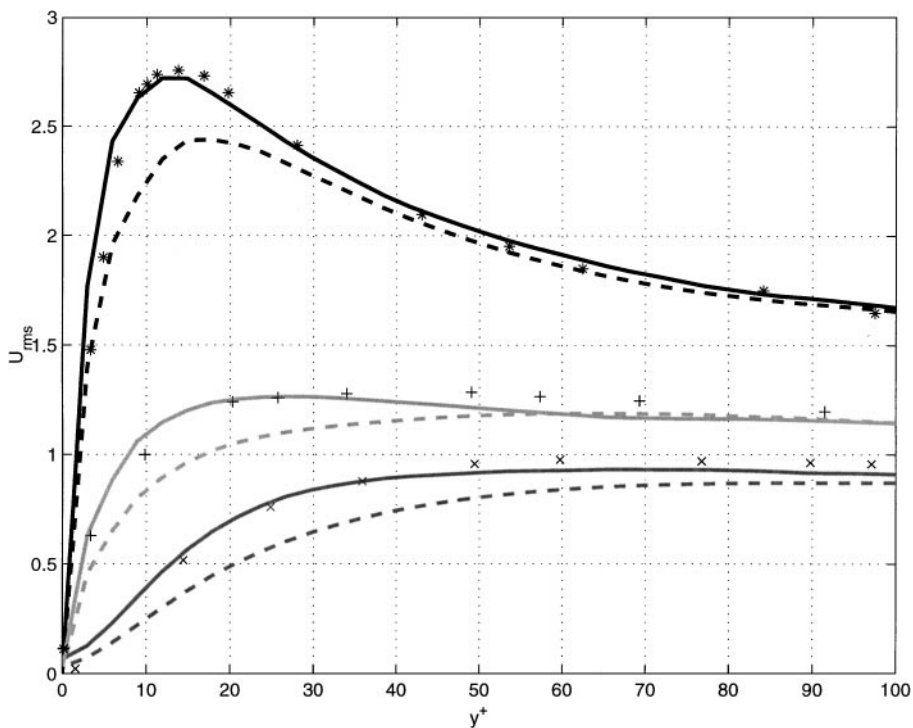


FIG. 17. $Re_\tau = 395$ simulations and comparisons with DNS: Turbulence intensities. Solid line—SVV; dashed line—spectral LES; points—Moser *et al.* [2].

Two simulations are presented, one with SVV and the other one following the classical LES approach; all discretization parameters are the same in the two simulations. A velocity field from a previous channel flow simulation at lower Reynolds number was interpolated to the new mesh. At this Reynolds number and for the resolution used, simulations without any SVV treatment were not possible; SVV was employed, with $\epsilon = 1/P$ and $M = 15$. It was compared to LES using the Smagorinsky model with $c_s = 0.032$, and the Panton wall-damping function in the near-wall region. Figure 17 shows turbulence intensities of the two simulations, compared with the DNS of Moser *et al.* Excellent agreement is achieved between the SVV simulation and DNS; however, the LES is over-dissipative in the near-wall region, while closer to the center line all the simulations converge.

6. SUMMARY AND DISCUSSION

The method presented here may be viewed as an *alternative LES* approach, in the sense of directly computing the large energetic scales while controlling the smaller scales via a spectral vanishing viscous (SVV) operator. The new second-order convolution operator introduced in the Navier–Stokes equations is parameterized by an amplitude ϵ and a spectral kernel Q . The latter selects which portion of the spectrum will be viscosity-free and which portion will be in the dissipative subrange. Both parameters depend on the local resolution, i.e., the number of modes. Their range is given by a theory for nonlinear conservation laws, first developed by Tadmor [22] and used mostly in solutions of 1-D and 2-D hyperbolic problems [28].

The new method can also be viewed as a hybrid approach between monotonicity-preserving schemes (like the PPM and FCT algorithms) and nonlinear Galerkin methods where the large and small scales are separated explicitly. Both of these schemes have been proposed as alternative LES for turbulence, and preliminary results have been encouraging [14, 16]. The important difference in the stability of the proposed SVV spectral/ hp method is that it is based on theoretical framework, even for the nonlinear case. Therefore, despite the extra SVV term in the Navier–Stokes equations, spectral convergence is preserved as shown in this paper (Section 4) in accordance with the theory.

Compared to traditional eddy-viscosity LES, the new method does not employ filtered equations, and this eliminates inaccuracies due to commutation errors associated with non-uniform grids. In addition, its computational complexity is insignificant compared to the eddy-viscosity or mixed-model LES. With respect to accuracy, the current results indicate that the SVV simulation results are better than the LES for channel flow, using in both cases spectral/ hp discretizations. However, many more numerical experiments are required to assess the accuracy of SVV simulations in turbulence. One of the problems with the SVV approach is that the viscosity kernel does not use information from the resolved scales directly. While this is true in the current implementation, in adaptive p-refinement the P modes per element will be changing dynamically to resolve the local flow physics. Therefore, in this case and depending on the implementation details, e.g., adaptive strategy, the SVV approach will incorporate physics for updating the spectral vanishing viscosity similar to those of the eddy-viscosity models in traditional LES. Such results will be reported in the future.

Another approach that will couple the SVV procedure to the dynamics of the flow can be formulated by considering the viscosity amplitude,

$$\epsilon = \frac{C(\mathbf{x}; t)}{P},$$

to be a function of position and time through the variable $C(\mathbf{x}; t)$. This variable can be selected *adaptively* by relating it to the dynamics of the flow, i.e., the strain field. More specifically, the following equation is proposed for Navier–Stokes,

$$C(\mathbf{x}, t) = \frac{\nu_e(\mathbf{x}; t)}{\nu},$$

where ν is the physical viscosity and ν_e is the eddy viscosity obtained, for example, by the Smagorinsky formula enhanced with the Panton modification for correct wall behavior. Clearly, at regions of low strain rates the effect of SVV is minimized and becomes zero right at the wall. In regions with high strain rate, C may achieve values larger than 1, which is consistent with the classical LES premise. The appropriate calibration of such a model should be tested via systematic simulations of various flows, but here we have revisited the inviscid Burgers equation presented in Section 3. The analog of the aforementioned idea is to scale the amplitude viscosity proportional to the magnitude of first derivative u_x , i.e.,

$$\epsilon_B \propto \frac{|u_x|}{|u_x|_\infty} \frac{1}{N}, \quad (12)$$

normalized with its maximum pointwise norm. Several such tests have been performed

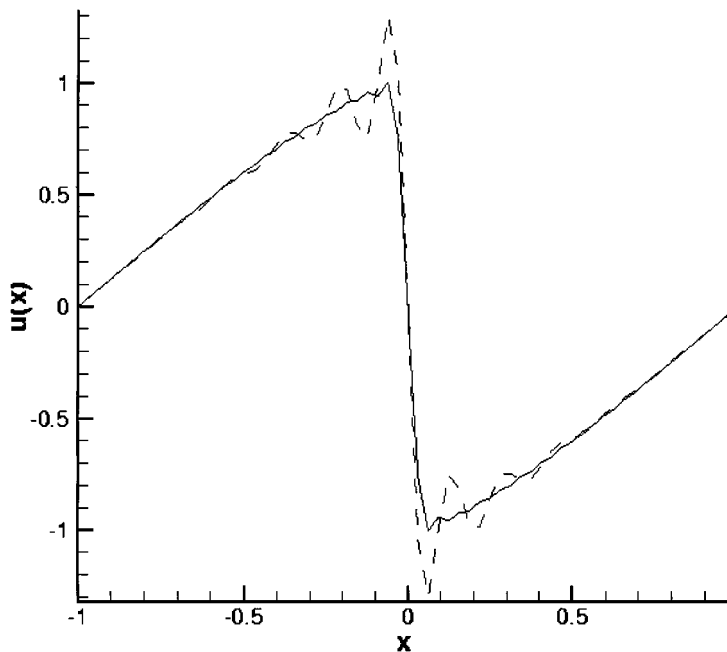


FIG. 18. Solution of inviscid Burgers equation using the proposed coupling procedure: Solid line— $C = 10|u_x|/|u_x|_\infty$; dashed line— $C = 10$.

and a typical result is shown in Fig. 18 for discretization with $N = 64$ modes. For this resolution, the Fourier method is unstable without any SVV treatment. Here we obtain solutions corresponding to constant $C = 10$ (dash line) and to C based on Eq. (12) and multiplied by 10. From this preliminary numerical result it can be seen that a better solution is clearly obtained with the proposed adaptive procedure around the discontinuity, whereas the smooth region is not affected. This solution is also improved compared to the solution corresponding to $C = 1$ shown in Fig. 3.

There are other open questions with the current SVV implementation that require resolution in the near future, which we list in the following:

- What is the relation between the SVV kernel and the hyperviscous kernel, and how is the quality of solutions affected in simulations of homogeneous turbulence?
- From the numerical point of view, can the SVV approach be extended to collocation methods and finite-difference methods, and what is the associated cost of computing the convolution operator?
- Can the SVV method be extended to compressible turbulence simulations, thus eliminating the often-used Favre approximate averaging procedure?
- Are the parameters ϵ and M employed in the numerical experiments in the current paper optimal, and what is their dependence on grid distortion and flow geometry?

Clearly, we do not have a definitive answer to these issues, and some of these questions are more difficult to answer than others as the preliminary simulation results of section 5.1.2 suggest. The one-dimensional version has already been extended to collocation methods [32], and the fact that the SVV is a second-order operator allows a straightforward implementation in finite element codes unlike hyperviscous kernels. On the other hand, at present

it is not clear how to develop rigorously the SVV method for finite difference methods avoiding the current empiricism, although some progress on this front has been made by employing similar ideas [47]. With regard to the parameter range, it is clear that studies more systematic than the ones presented in Section 5.1.2 are needed to answer questions of optimality and dependence on the flow geometry.

APPENDIX I

The Spectral/ hp Method

The main discretization concepts of the spectral/ hp method are reviewed in the context of the 1-D inviscid Burgers equation enhanced with the SVV second-order operator. The objective is to introduce the hierarchical trial basis of the method which is derived from Jacobi polynomials and to discuss some of the implementation details.

Equation (1) is considered, in a domain $-1 \leq x \leq 1$, with a Dirichlet boundary condition and a Neumann boundary condition; i.e., $u(-1, t) = g$, $u'(1, t) = h$. The initial condition is a sine wave $u(x, 0) = \sin(\pi x)$. The residual of Eq. (3) is

$$R(u) = \int_{\Omega} w \left[\epsilon \frac{\partial}{\partial x} \left[Q_{\epsilon} \frac{\partial u}{\partial x} \right] - \frac{\partial}{\partial t} u(x, t) - \frac{\partial}{\partial x} \left(\frac{u^2(x, t)}{2} \right) \right] dx, \quad (13)$$

where u is the *trial solution*, the set of which is denoted by S , and $w \in \mathcal{V}$ is a test function. Each test function should satisfy $w(-1) = 0$ and be homogeneous on a Dirichlet boundary. Here the spaces are defined as

$$S = \{u \mid u \in H^1, u(-1) = g\}, \quad \mathcal{V} = \{w \mid w \in H^1, w(-1) = 0\}.$$

Integrating Eq. (13) once by parts and setting $R(u) = 0$ give

$$\epsilon w(1) Q_{\epsilon} h - \int_{\Omega} \epsilon w' Q_{\epsilon} u' dx - \int_{\Omega} w \left[\frac{\partial}{\partial t} u(x, t) + \frac{\partial}{\partial x} \left(\frac{u^2(x, t)}{2} \right) \right] dx = 0.$$

Introducing the notation

$$\begin{aligned} a(w, u) &= \int_{\Omega} \epsilon Q_{\epsilon} \frac{\partial w}{\partial x} \frac{\partial u}{\partial x} dx, \\ f(w) &= - \int_{\Omega} w \left[\frac{\partial}{\partial t} u(x, t) + \frac{\partial}{\partial x} \left(\frac{u^2(x, t)}{2} \right) \right] dx, \end{aligned} \quad (14)$$

the above equation may be rewritten as

$$a(w, u) = f(w) + \epsilon Q_{\epsilon} w(1) h. \quad (15)$$

Searching for solutions in finite subspaces, i.e., $S^h (S^h \subset S)$, $\mathcal{V}^h (\mathcal{V}^h \subset \mathcal{V})$, Eq. (15) may be rewritten as

$$a(w^h, u^h) = (w^h, f) + \epsilon Q_{\epsilon} w^h(1) h. \quad (16)$$

Thus, the function u^h is decomposed into a known component, u^{hD} , which satisfies the Dirichlet boundary condition and lies in the trial space, and an unknown term, u^{hH} , which lies in the test space and is zero on the Dirichlet boundary; i.e., $u^h = u^{hD} + u^{hH}$. By reducing an infinite-dimensional problem to an n -dimensional one, each member of S^h and \mathcal{V}^h is represented by a set of n basis functions $(\phi_1, \phi_2, \dots, \phi_n)$, $\phi_p(0) = 0$, admitting all linear combinations; i.e., $w^h = c_1\phi_1 + c_2\phi_2 + \dots + c_n\phi_n$. Also, $u^h = u^{hD} + u^{hH} = g\phi_{n+1} + \sum_{p=1}^n d_p\phi_p$, $\phi_{n+1}(0) = 1$. Substituting u^h for u and w^h for w , Eq. (16) takes the form

$$\sum_{p=1}^n c_p G_p = 0,$$

where

$$G_p = \sum_{q=1}^n a(\phi_p, \phi_q) d_q - (\phi_p, f) - \epsilon Q_\epsilon \phi_p(1)h + a(\phi_p, \phi_{n+1})g.$$

Since this is true for any c_p , G_p is necessarily equal to 0 and the above equation may be rewritten as

$$\sum_p \left(\sum_{q=1}^n \epsilon Q_\epsilon d_q \phi_p' \phi_q' - \phi_p f - \epsilon Q_\epsilon \phi_p(1)h + \epsilon Q_\epsilon \phi_p' \phi_{n+1}' g \right) = 0. \quad (17)$$

Equivalently to the Fourier representation of Tadmor [22], Q_N (which will replace Q_ϵ in the above expression) may be approximated by a kernel Q_p , of the form

$$Q_p = e^{-\frac{(p-P)(p-P)}{(p-m_p)(p-m_p)}}, \quad m_p < p \leq P. \quad (18)$$

In essence, the multiplication of Fourier coefficients, in the Fourier method, is translated into a multiplication of modal coefficients, hence an introduction of dissipation at the high modes. Equation (17), therefore, takes the form

$$\sum_p \left(\sum_{q=1}^n d_q \epsilon Q_p Q_q \phi_p' \phi_q' - \phi_p f - \epsilon Q_p \phi_p(1)h + \epsilon Q_p Q_{n+1} \phi_p' \phi_{n+1}' g \right) = 0. \quad (19)$$

The computational domain is subsequently divided into a number of elements k . On each element, a set of local functions is introduced that provide p th order accuracy for the solution over the k th element. In spectral/hp methods, these local functions are called *basis functions* and are invariably polynomials.

The modal expansions adopted in this work are Jacobi polynomials, $P_p^{\alpha, \beta}(x)$ [29]. Jacobi polynomials are the family of polynomial solutions to a singular Sturm–Louville problem and, for $-1 < x < 1$, can be written as

$$\frac{d}{dx} \left[(1-x)^{1+\alpha} (1+x)^{1+\beta} \frac{d}{dx} u_p(x) \right] = \lambda_p (1-x)^\alpha (1+x)^\beta u_p(x),$$

with $u_p(x) = P_p^{\alpha, \beta}(x)$, $\lambda_p = -p(\alpha + \beta + p + 1)$. Jacobi polynomials have the

orthogonality property

$$\int_{-1}^1 (1+x)^\beta (1-x)^\alpha P_p^{\alpha,\beta}(x) P_q^{\alpha,\beta}(x) dx = C \delta_{pq}$$

with C depending on α, β, p . Thus, $P_p^{\alpha,\beta}(x)$ is orthogonal to all polynomials of order less than p when integrating with $(1+x)^\beta (1-x)^\alpha$ and the modal expansion basis is then defined as

$$\begin{aligned} \phi_p(\xi) &= \frac{1}{4}(1-\xi)(1+\xi)P_{p-2}^{1,1}(\xi), & 0 < p < P \\ \phi_0(\xi) &= \frac{1-\xi}{2}, & p = 0 \\ \phi_P(\xi) &= \frac{1+\xi}{2}, & p = P \end{aligned} \quad (20)$$

in the standard interval $\Omega = \{\xi \mid -1 < \xi < 1\}$.

Unlike the nodal basis where every basis function is an N th-order polynomial, in the modal basis there is a hierarchy of modes starting from the linear, proceeding with the quadratic, cubic, etc. (Fig. 19).

Returning to the Burgers equation, Eq. (17) may be rewritten in matrix form as

$$\begin{aligned} [A]\underline{x} &= \underline{B} \\ \underline{B} &= \phi_p f + \epsilon Q_p \phi_p(1)h - \epsilon Q_p Q_{n+1} \phi'_p \phi'_{n+1} g \\ [A] &= \epsilon Q_p Q_q \phi'_p \phi'_q \\ \underline{x} &= \underline{d}_q, \end{aligned} \quad (21)$$

where $[A]_{pq}^k = \int_{\Omega} \epsilon Q_p Q_q \phi'_p \phi'_q dx$.

So far only one element has been considered and thus convergence depends solely on the increase in the polynomial order. Extending the above to multiple element domains with varying coordinate systems requires a procedure to transform the elemental matrices $[A]$, \underline{x} , \underline{B} to their equivalent submatrices in the global multielement domain. The global element

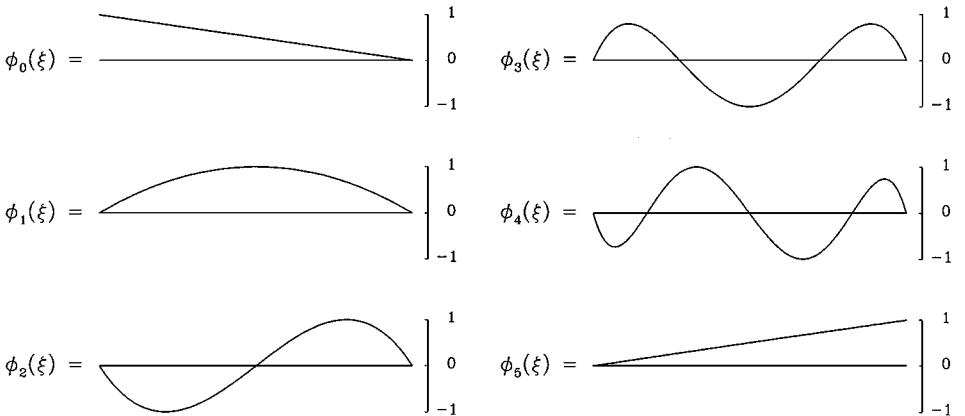


FIG. 19. Shape of modal expansion modes for a polynomial order of polynomial order $P = 5$.

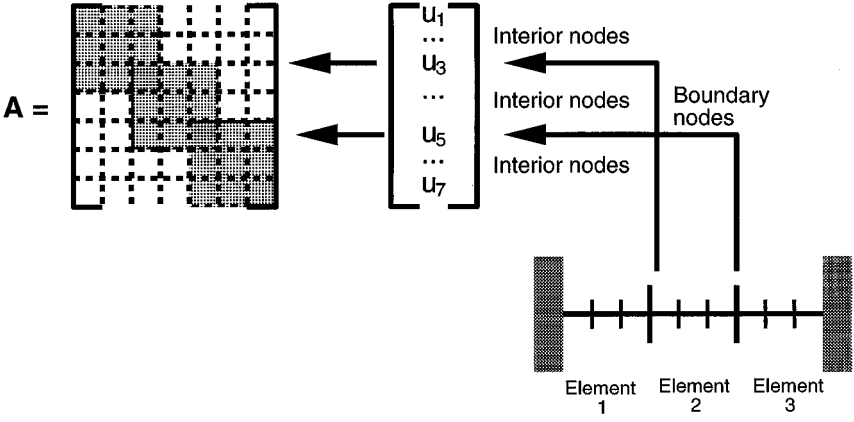


FIG. 20. Schematic of direct stiffness summation of local matrices to form the global matrix A .

Ω_g can be mapped to any elemental (or local) domain Ω_l via the transformation $X_e(\xi)$ which expresses the global coordinate x in terms of the local coordinate ξ ; i.e.,

$$x = X_e(\xi) = \frac{1 - \xi}{2} x_{e-1} + \frac{1 + \xi}{2} x_e, \quad \xi \in \Omega_g.$$

Therefore, the global expansion basis takes the form

$$\begin{aligned} \Phi_p(x) &= \phi(X_e(\xi)), \\ \Phi'_p(x) &= \frac{\partial \Phi}{\partial x} = \phi'_p(\xi) \frac{\partial \xi}{\partial x}, \end{aligned} \quad (22)$$

where $\frac{\partial \xi}{\partial x} = J^{-1}$, with J the Jacobian. Once all the local matrices have been transformed to global submatrices they need to be assembled, by summing contributions from the elemental matrices. The procedure is illustrated in Fig. 20.

Matrix $[A]$ is banded as a result of using local basis functions, with its nonzero entries located in the N diagonals above and below the main diagonal. Each element is placed on the matrix, as shown in Fig. 20, with the edges of each element added to the neighboring elements. Due to the Galerkin approximation, matrix $[A]$ is also symmetric and positive definite.

The main aspects of spectral/ hp method have been presented through the example of the solution of a 1-D Burgers equation. This may be summarized as:

1. Determine the number of elements and the number of modes.
2. Determine the global coordinates x .
3. Determine the local to global transformation matrix.
4. Calculate the elemental matrices $[A]$, \underline{x} , \underline{B} for each element and transform the elemental matrices to global sub-matrices.
5. Assemble the global matrices.
6. Solve the system of equations $[A]\underline{x} = \underline{B}$.
7. Form the solution $u(x) = \sum_{k=0}^{n_{nel}-1} \sum_{i=0}^{n_m-1} \hat{u}_i \Phi_i(x)$.

It should be mentioned that when the Dirichlet boundary conditions are used, the rows and columns containing the corresponding Dirichlet boundary points are not included

when inverting the matrix $[A]$, since they have been condensed out and are included in \underline{B} .

APPENDIX II

Time-Stepping Scheme

For the temporal discretization of the Navier–Stokes equations we use a standard Adams–Bashforth/Crank–Nicolson algorithm (a theta scheme) with an improved pressure boundary condition to enhance the temporal accuracy [48], as

$$\begin{aligned} \frac{\hat{\mathbf{V}} - \mathbf{V}^n}{\Delta t} &= \sum_{q=0}^{J_e-1} \beta_q [-(\mathbf{V} \cdot \nabla) \mathbf{V}]^{n-q} \\ \nabla^2 p^{n+1} &= \nabla \cdot \left(\frac{\hat{\mathbf{V}}}{\Delta t} \right) \\ \nu \nabla^2 \mathbf{V}^* - \frac{1}{\Delta t(1-\theta)} \mathbf{V}^* &= -\frac{\hat{\mathbf{V}} + \frac{\theta}{1-\theta} \mathbf{V}^n}{\Delta t}, \end{aligned} \quad (23)$$

where $\hat{\mathbf{V}} = \hat{\mathbf{V}} + \Delta t \nabla p^{n+1}$ and $\mathbf{V}^* = (\mathbf{V}^n + \mathbf{V}^{n+1})/2$. The pressure equation is supplemented with the boundary condition

$$\frac{\partial p^{n+1}}{\partial \mathbf{n}} = n \cdot \left[-\sum_{q=0}^{J_e-1} \beta_q [(\mathbf{V} \cdot \nabla) \mathbf{V}] \right] - n \cdot \left[\sum_{q=0}^{J_e-1} \beta_q [\nu \nabla \times (\nabla \times \mathbf{V})]^{n-q} \right].$$

In order to efficiently implement the SVV method, the SVV term $\epsilon \nabla(Q_\epsilon \nabla \mathbf{V})$ may be included in the Helmholtz equation; therefore, the Helmholtz equation takes the form

$$\epsilon \nabla(Q_\epsilon \nabla \mathbf{V}^*) + \nu \nabla^2 \mathbf{V}^* - \frac{1}{\Delta t(1-\theta)} \mathbf{V}^* = -\frac{\hat{\mathbf{V}} + \frac{\theta}{1-\theta} \mathbf{V}^n}{\Delta t}. \quad (24)$$

APPENDIX III

Subfilter Model

The spectral LES formulation used is briefly reviewed in the results presented in the current work as there is a new issue not presented elsewhere before: that of the appropriate length scale in a multiresolution method as the spectral hp method. The equations of motion for a large-eddy simulation are

$$\frac{\partial(\tilde{u}_i)}{\partial x_i} = 0, \quad \frac{\partial(\tilde{u}_i)}{\partial t} + \frac{\partial(\tilde{u}_i \tilde{u}_j)}{\partial x_j} = -\frac{\partial \tilde{p}}{\partial x_i} + \frac{\partial}{\partial x_i} \left\{ (\nu + \nu_s) \left[\frac{\partial \tilde{u}_i}{\partial x_j} + \frac{\partial \tilde{u}_j}{\partial x_i} \right] \right\}, \quad (25)$$

where the term ν_s represents the Smagorinsky eddy-viscosity model, defined as $\nu_s = l_s^2 |\tilde{S}|$, with $|\tilde{S}| = (2\tilde{S}_{ij}\tilde{S}_{ij})^{1/2}$ the magnitude of the filtered strain-rate tensor. Here, l_s is the *Smagorinsky length scale* or *subfilter length scale*. It is equal to $l_s = c_s \Delta$, where c_s is

the *Smagorinsky constant*, and Δ is the filter width. In structured grids typically $\Delta = (\Delta_x \Delta_y \Delta_z)^{1/3}$, where Δ_x , Δ_y , Δ_z are the filter widths in each direction. For the spectral/*hp* method on quadrilateral and triangular prisms with Fourier expansions along the streamwise (x direction), the filter width Δ has to be defined properly in order to account for the *subcell resolution*. Following the heuristic argument in [49], the polynomial order, P , and resolved half-wave number, k , are related by $P = k\pi$. A new definition of Δ is thus proposed based on the area of the triangle, A , and the grid spacing, Δx , in the Fourier direction, of the form

$$\Delta = \left(A \left(\frac{\pi}{P} \right)^2 \Delta x \right)^{1/3}. \quad (26)$$

Numerical experiments with decaying homogeneous turbulence and turbulent channel flow have justified this choice (see [40, 50]). In the near-wall region, the Panton [44] wall-damping function is used which follows the correct shear stress y^3 asymptotic behavior in the near wall. Spectral element/*hp*-LES based on this choice of subfilter behaves similar to standard LES but because of the dual path of convergence, i.e., reducing the element size or increasing the polynomial order, more flexibility and better diagnostics of underresolution are available.

ACKNOWLEDGMENTS

We thank Professors Eitan Tadmor and David Gottlieb for their helpful suggestions. We also acknowledge the help of R. M. Kirby and Xu Jin for additional computations suggested by the referees. This work was supported by AFOSR, ONR, DOE and NSF, and computations were done on the the SGI O 2000 at NCSA (University of Illinois, Urbana-Champaign), on the IBM SP2 at MHPCC (University of New Mexico), and on the IBM SP2 at CASCV (Brown University).

REFERENCES

1. J. W. Deardorff, A numerical study of three-dimensional turbulent channel flow at large Reynolds numbers, *J. Fluid Mech.* **41**(2), 453 (1970).
2. R. D. Moser, J. Kim, and N. N. Mansour, Direct numerical simulation of turbulent channel flows up to $Re_\tau = 590$, *Phys. Fluids* **11**(4) (1999).
3. C. Meneveau, Statistics of turbulence subgrid-scale stresses: Necessary conditions and experimental tests, *Phys. Fluids* **6**, 815 (1994).
4. V. Borue and S. A. Orszag, Local energy flux and subgrid-scale statistics in three-dimensional turbulence, *J. Fluid Mech.* **366**, 1 (1998).
5. G. E. Karniadakis and G. L. Brown, Vorticity transport in modeling three-dimensional unsteady shear flows, *Phys. Fluids* **7**(4), 688 (1995).
6. M. Lesieur and O. Metais, New trends in large-eddy simulation, *Annu. Rev. Fluid Mech.* **28**, 45 (1996).
7. J. Bardina, Improved Turbulence Models Based on Large Eddy Simulation of Homogeneous Incompressible Turbulent Flows, Ph.D. thesis (Stanford University, 1983).
8. M. V. Salvetti and S. Banerjee, A priori tests of a new dynamic subgrid-scale model for finite-difference large-eddy simulations, *Phys. Fluids* **7**, 2831 (1995).
9. K. Horiuti, A new dynamic two-parameter mixed model for large-eddy simulation, *Phys. Fluids* **9**, 3443 (1997).
10. T. Dubois, F. Jauberteau, and R. Temam, Solution of the incompressible Navier–Stokes equations by the nonlinear Galerkin method, *J. Sci. Comp.* **8**, 167 (1993).
11. T. J. R. Hughes, L. Mazzei, and K. E. Jansen, Large-eddy simulation and the variational multiscale method. Submitted for publication.

12. D. H. Porter, A. Pouquet, and P. R. Woodward, Kolmogorov-like spectra in decaying three-dimensional supersonic flows, *Phys. Fluids* **6**, 2133 (1994).
13. J. P. Boris, F. F. Grinstein, E. S. Oran, and R. J. Kolbe, New insights into large eddy simulation, *Fluid Dyn. Res.* **19**, 19 (1992).
14. C. Fureby and F. F. Grinstein, Monotonically integrated large eddy simulation of free shear flows, *AIAA J.* **37**(5), 544 (1999).
15. J.-L. Guermond, Subgrid stabilisation of Galerkin approximations of monotone operators, in *Proceedings of the European Science Foundation Conference on Applied Mathematics for Industrial Flow Problems (AMIF) (San Felu de Guixols, Costa Brava, 1998)*.
16. G. Urbin and D. Knight, Large eddy simulation of the interaction of a turbulent boundary layer with a shock wave using unstructured grids, in *Second AFSOR International Conference on DNS and LES* (Rutgers Univ. Press, New Brunswick, NJ, 1999).
17. R. J. LeVeque, *Numerical Methods for Conservation Laws*, 2nd ed. (Birkhuser-Verlag, Berlin, New York, 1992).
18. I. G. Giannakouros and G. E. Karniadakis, A spectral element-FCT method for the compressible Euler equations, *J. Comput. Phys.* **115**, 65 (1994).
19. E. S. Oran and J. P. Boris, *Numerical Simulation of Reactive Flow* (Elsevier, Amsterdam/New York 1987).
20. P. D. Lax, Hyperbolic systems of conservation laws and the mathematical theory of shock waves, in *ABMS-NSF Regional Conference Series in Applied Mathematics 11, Society for Industrial and Applied Mathematics* (Philadelphia, PA, 1972).
21. S. K. Godunov, A difference method for numerical calculation of discontinuous solutions of the equations of hydrodynamics, *Mat. Sb* **47**, 271 (1959).
22. E. Tadmor, Convergence of spectral methods for nonlinear conservation laws, *SIAM J. Numer. Anal.* **26**(1), 30 (1989).
23. Y. Maday and E. Tadmor, Analysis of the spectral viscosity method for periodic conservation laws, *SINUM* **26**, 854 (1989).
24. E. Tadmor, Super viscosity and spectral approximations of nonlinear conservation laws, in *Numerical Methods for Fluid Dynamics, IV*, edited by M. J. Baines and K. W. Morton (Clarendon Press, Oxford, 1993), p. 69.
- 24a. G.-Q. Chen, Q. Dy, and E. Tadmor, Spectral viscosity approximations to multidimensional scalar conservation laws, *Math. Comp.* **61**, 629 (1993).
25. H.-P. Ma, Chebyshev–Legendre spectral viscosity method for nonlinear conservation laws, *SIAM J. Numer. Anal.* **35**(3), 901 (1998).
26. H.-P. Ma, Chebyshev–Legendre super spectral viscosity method for nonlinear conservation laws, *SIAM J. Numer. Anal.* **35**(3), 903 (1998).
27. Ø. Andreassen, I. Lie, and C. E. Wasberg, The spectral viscosity method applied to simulation of waves in a stratified atmosphere, *J. Comput. Phys.* **110**, 257 (1994).
28. S. M. O. Kaber, A Legendre pseudospectral viscosity method, *J. Comput. Phys.* **128**, 165 (1996).
29. G. E. Karniadakis and S. J. Sherwin, *Spectral/hp Element Methods for CFD* (Oxford Univ. Press, London, 1999).
30. W. S. Don, Numerical study of pseudospectral methods in shock wave applications, *J. Comput. Phys.* **110**, 103 (1994).
31. M. G. Crandall and P. L. Lions, Viscosity solutions of Hamilton–Jacobi equations, *Trans. Am. Math. Soc.* **61**, 629 (1983).
32. Y. Maday, S. M. Ould Kaber, and E. Tadmor, Legendre pseudospectral viscosity method for nonlinear conservation laws, *SIAM J. Numer. Anal.* **30**, 321 (1993).
33. E. Tadmor, Total variation and error estimates for spectral viscosity approximations, *Math. Comp.* **60**, 245 (1993).
34. M. Lesieur and O. Metais, New trends in large-eddy simulation, *Ann. Rev. Fluid Mech.* **28**, 45 (1996).
35. R. H. Kraichnan, Eddy viscosity in two and three dimensions, *J. Atmos. Sci.* **33**, 1521 (1976).

36. J. P. Chollet, Two-point closures as a subgrid scale modelling for large eddy simulations, in *Turbulent Shear Flows IV*, edited by F. Durst and B. Launder (Springer-Verlag, Berlin/New York, 1984).
37. L. Emmel, Methode spectrale multidomaine de viscosite evanescente pour des problems hyperboliques non lineaires, Ph.D. thesis (University of Paris 6, France, 1998).
38. D. Gottlieb and C.-W. Shu, On the Gibbs phenomenon and its resolution, *SIAM Review* **39**, 644 (1998).
39. A. Gelb and E. Tadmor, Detection of edges in spectral data, *Appl. Comput. Harmonic Anal.* **7**, 101 (1999).
40. G.-S. Karamanos, Large-Eddy Simulation Using Unstructured Spectral/hp Elements, Ph.D. thesis (Imperial College, Department of Aeronautics, 1999).
41. J. Kim, P. Moin, and R. Moser, Turbulence statistics in fully developed channel flow at low Reynolds number, *J. Fluid Mech.* **117**, 133 (1987).
42. U. Piomelli, Models for Large Eddy Simulations of Turbulent Flow including Transpiration, Ph.D. thesis (Stanford University, 1987).
43. M. Wille, Large Eddy Simulation of Jets in Cross Flows, Ph.D. thesis (Imperial College, Department of Chemical Engineering, 1997).
44. R. L. Panton, A Reynolds stress function for wall layers, *J. Fluids Eng.* **119**, 325 (1997).
45. H. P. Kreplin and H. Eckelmann, Behaviour of the three fluctuating velocity components in the wall region of a turbulent channel flow, *Phy. Fluids* **22**(7), 1233 (1979).
46. R. Temam, Approximation of attractors, large eddy simulations and multiscale methods, *Proc. R. Soc. Lond.* **434**, 23 (1991).
47. C. K. W. Tam, J. C. Webb, and Z. Dong, A study of the short wave components in computational acoustics, *J. Comput. Acoustics* **1**, 1 (1993).
48. G. E. Karniadakis, M. Israeli, and S. A. Orszag, High-order splitting methods for incompressible Navier-Stokes equations, *J. Comput. Phys.* **97**, 414 (1991).
49. D. Gottlieb and S. A. Orszag, Numerical analysis of spectral methods: Theory and applications, in *SIAM-CMBS* (Soc. for Industr. & Appl. Math., Philadelphia, 1977).
50. G.-S. Karamanos, S. J. Sherwin, and J. F. Morrison, Large-eddy simulation using unstructured spectral/hp elements, in *Recent Advances in DNS and LES*, edited by D. Knight & L. Sakell (Kluwer Academic, Dordrecht/Norwell, MA, 1999).